Journal of ELECTRONIC MATERIALS
DOI: 10.1007/s11664-012-1990-0
© 2012 TMS

Modulation Transfer Function Measurement of Infrared Focal-Plane Arrays with Small Fill Factors

FLORENCE de la BARRIÈRE,[1,3] GUILLAUME DRUART,[1] NICOLAS GUÉRINEAU,[1] SYLVAIN ROMMELUÈRE,[1] LAURENT MUGNIER,[1] OLIVIER GRAVRAND,[2] NICOLAS BAIER,[2] NICOLAS LHERMET,[2] GÉRARD DESTEFANIS,[2] and SOPHIE DERELLE[1]

1.—Onera—The French Aerospace Laboratory, Chemin de la Hunière, 91761 Palaiseau Cedex, France. 2.—CEA LETI MINATEC, 17 rue des Martyrs, 38054 Grenoble Cedex 9, France. 3.—e-mail: florence.de_la_barriere@onera.fr

This paper describes an original method to measure the modulation transfer function (MTF) of an infrared focal-plane array (IRFPA), based on a diffraction grating called a continuously self-imaging grating (CSIG). We give a general methodology to design the test bench, and we describe the data processing approach which has been developed to extract relevant information about the size of the photodiodes and filtering effects. The MTF measurement capability of this method is illustrated with a cooled IRFPA.

Key words: Modulation transfer function, infrared focal-plane arrays, small fill factor pixels, digital image processing

INTRODUCTION

Measuring the spatial response of the pixels of a focal-plane array (FPA) is of great interest: on the one hand, the technologist could check the quality of the pixels and study phenomena related to detection, such as scattering or cross-talk between adjacent pixels, and on the other hand, the optical designer could evaluate the impact of the spatial filtering of the pixels on image quality. An adequate figure of merit which accounts for filtering effects of pixels in the Fourier domain is the modulation transfer function (MTF). Indeed, it quantifies the ability of the FPA to reproduce successfully the spatial frequency content of the scene.

Several techniques have been developed for measuring the MTF of FPAs: local methods consist in analyzing the pixel response to a point source or to a line source for each pixel of the FPA; on the contrary, global methods provide MTF measurement in a single acquisition assuming that all the pixels of the FPA are identical.

Local methods use a canted knife edge,[1] a canted slit,[2,3] a scanning line source,[4] or a scanning point source.[5] All these techniques involve a high-quality and high-aperture lens to image patterns of interest on the FPA, so that the resolution of the measurement remains unaffected by the point spread function of the projection device. Moreover, scanning techniques require precision mechanical devices to move these systems.

Global methods rely on the projection of a pattern with known properties on the FPA. This pattern can be either interferometric fringes,[6–8] a speckle pattern,[9–11] a random target,[12] or a periodic pattern with known spatial frequencies.[13,14] Their main advantage is that they require neither high-precision optical components nor critical alignment, and the measurement can be carried out in a single acquisition in most cases. However, advanced data post-processing methods have to be associated with these techniques to extract MTF information.

During the past years, we have proposed a set of improved measurement methods for evaluating the MTF of FPAs. The principle is to project a high-resolution periodic target on the FPA, using the self-imaging property (known as Talbot effect) of a grating illuminated by a plane wave. The main advantage of this method is that no optics is required to project the target.[15,16] Then, we introduced a new type of optical element, called nondiffracting arrays,

(Received October 10, 2011; accepted February 6, 2012)

Published online: 29 February 2012

which produce nondiffracting beams. One of these nondiffracting arrays is a two-dimensional diffraction grating, called a continuously self-imaging grating (CSIG),[17] which can be used for MTF measurement. When illuminated by a plane wave, a CSIG produces a field whose intensity profile is a propagation- and wavelength-invariant biperiodic array of bright spots.[18,19] In this paper, we take advantage of this property of CSIGs to measure the spatial response of FPAs. Indeed, a CSIG is a component which is particularly well suited for designing a simple test bench, since it does not require any precise focusing distance; that is to say, it is not necessary to control precisely the distance between the CSIG and the FPA. This is a huge advantage for MTF measurement of HgCdTe infrared FPAs (IRFPAs), since such detectors need to be integrated in a sealed and cooled vacuum chamber called a Dewar.

In previous work,[20] we showed a first example of MTF measurement using a CSIG. The aim of this paper is to relate the improvements of this method over the past years. In this paper, we provide a deeper description of the test bench, as well as a new and more efficient data processing method. In "An IRFPA Manufactured to Obtain Pixels with Small Fill Factors" section we describe the main features of the IRFPA which has been made for the purpose of carrying out MTF measurements: it is composed of several zones with varying small fill factors for the pixels. In "Methodology to Design a Simple MTF Measurement Bench Based on a CSIG" section we focus on the design of the test bench used for MTF measurement with a CSIG. "Data Processing and Experimental Results" section presents the data processing method which has been developed to extract MTF information and the experimental results obtained with the original IRFPA under study.

AN IRFPA MANUFACTURED TO OBTAIN PIXELS WITH SMALL FILL FACTORS

We have designed and manufactured a specific cooled (77 K) IRFPA based on HgCdTe technology, working in the [3 μm; 5 μm] spectral range. This IRFPA is composed of 320 $\times$ 256 pixels and is divided into nine areas: the pixel pitch is the same for all areas (3 μm), the only difference being the fill factor, which differs from one zone to another. Thus, a single IRFPA allows testing and measuring several technological parameters for the photodiodes at the same time. When the IRFPA is illuminated with black-body radiation, the different zones clearly appear (Fig. 1): the different current levels are due to different fill factors. The central zone (zone 5) corresponds to standard infrared pixels with fill factor equal to 1. The other zones correspond to pixels with fill factors inferior to 1. To obtain the small fill factors, two approaches are studied: in the first one, the photodiode is implanted on a diameter equal to Φ_D and it is not confined, while in the second one, the photodiode is implanted on a diameter equal to Φ_D and a circular confinement ring (diameter Φ_{CR}) surrounds the tested diode (Fig. 2). The technological parameters Φ_D and Φ_{CR} used for the different zones are listed in Table I. Depending on the values of these parameters, we expect to obtain different effective active areas for the diodes. Two main reasons can be provided to explain why we chose to make circular photodiodes. Firstly, photolithography tends to make the edges of small patterns round. Indeed, even if the patterns on the mask are square, photolithography makes the printed small patterns round rather than square.

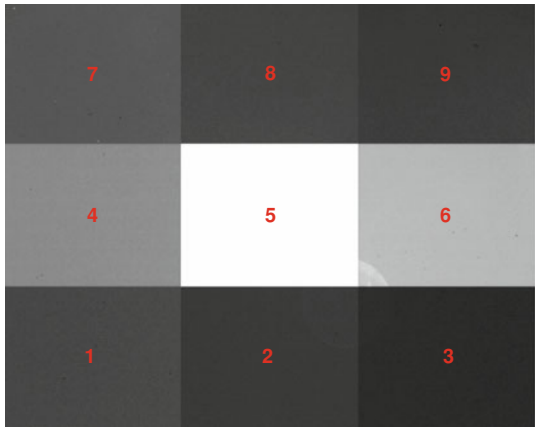

Fig. 1. Response of the HgCdTe IRFPA to black-body radiation at 298 K (the number of each zone is indicated). The different current levels are due to different fill factors.

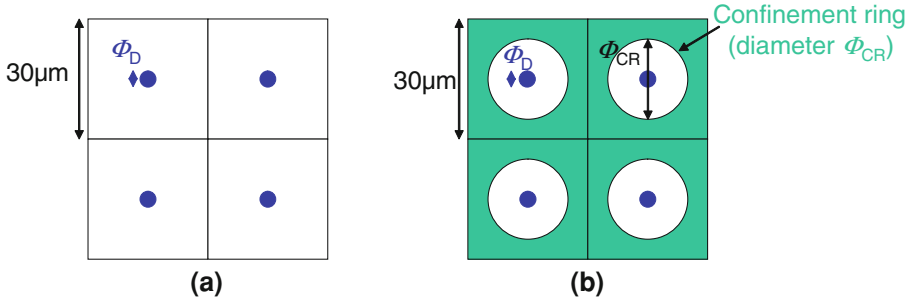

Fig. 2. Illustration of the two approaches applied to obtain small fill factors: (a) the diode is implanted on diameter Φ_D and is not confined, (b) the diode is implanted on diameter Φ_D and a confinement ring (diameter Φ_{CR}) surrounds the tested diode.

Table I. Technological parameters for the different zones of the IRFPA. For zone 5, the pixels are square (30 μm × 30 μm) with fill factor equal to 1

Zone	1	2	3	4	5	6	7	8	9
Diode diameter, Φ_D (μm)	2	2	2	2	–	3	3	3	3
Confinement ring diameter, Φ_{CR} (μm)	18	14	10	No ring	–	No ring	17	13	11

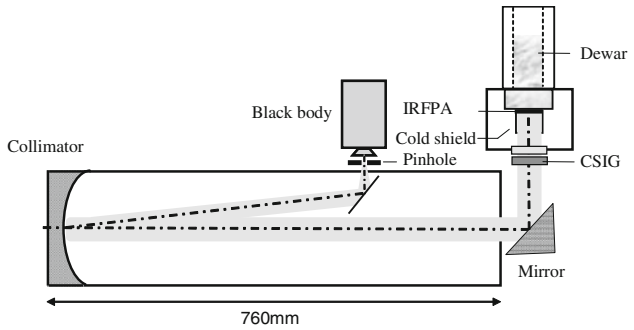

Fig. 3. Experimental setup for measurement of the MTF of a cooled IRFPA with a CSIG.

Secondly, for the zones where the photodiodes are not confined, the shape of the effective active area of the photodiode is given by the convolution of the pattern of the photodiode and of the diffusion zone. The diffusion zone is circular, so the effective active area of the photodiode tends to be circular.

METHODOLOGY TO DESIGN A SIMPLE MTF MEASUREMENT BENCH BASED ON A CSIG

General Description of the Test Bench

As the light source, we use a black body at temperature T = 1473 K. This black body illuminates a pinhole which is placed at the focal point of a collimator with focal length f = 760 mm. This setup generates a polychromatic infrared plane wave at the exit of the collimator. The CSIG is placed just in front of the window of the Dewar which contains the IRFPA. The test bench is illustrated in Fig. 3.

Choosing the CSIG

CSIGs are diffraction gratings which belong to the class of continuously self-imaging objects.[21] When illuminated by a plane wave, they produce a field whose intensity profile is a propagation- and wavelength-invariant biperiodic array of bright spots (Fig. 4). A detailed description of CSIGs and of their properties can be found in Refs. 17 and 18. In this subsection, we only recall fundamental features of CSIGs, which are directly used to design the MTF measurement test bench. First of all, it is worth mentioning that a CSIG is a periodic target, and therefore, it excites a set of discrete spatial frequencies in the Fourier domain. By choosing properly the period of the grating and its orientation with respect to the pixel lines of the detector, aliased spatial frequencies are folded onto frequencies of null amplitude, thus enabling MTF measurement beyond the Nyquist frequency of the IRFPA.

The radius r_0 of the spots produced by a CSIG is given by Ref. 17 as

$$r_0 = 0.38 a_0/\eta, \tag{1}$$

where a_0 is the distance between two consecutive bright spots (i.e., the period of the CSIG), and η is a dimensionless scaling factor.

The pattern produced by a CSIG (illustrated in Fig. 4c) excites discrete spatial frequencies widely spread in the Fourier domain (Fig. 5). All these excited spatial frequencies are contained in a circle of radius v_c given by

$$v_c = 2\eta/a_0. \tag{2}$$

v_c corresponds to the maximal spatial frequency which can be measured with a CSIG with parameters η and a_0.

When varying η, the number of orders diffracted by the CSIG changes. The CSIG we used for the measurements diffracts 24 orders (which corresponds to $\eta = \sqrt{650}$), and its period is equal to a_0 = 1 mm. Then, the maximal spatial frequency which can be measured is equal to v_c = 50 cycles/mm.

Choosing the Diameter of the Pinhole

We chose to use a pinhole for the illumination because it could enable two-dimensional measurements of the MTF of the FPA. Great care must be taken when choosing the diameter Φ of the pinhole: if the pinhole is too large, it affects the size of the projected pattern because it induces an additional and undesired filtering effect in the final image. The diameter Φ' of the image of the pinhole on the detector is given by

$$\Phi' = \Phi \frac{d}{f}, \tag{3}$$

where d is the distance between the IRFPA and the CSIG. For our experimental setup, d mainly depends on the height of the Dewar roof, and thus cannot be reduced to extremely small values. We measured d directly on our test bench as d = 15 mm.

The filtering function F_{pinhole} induced by the pinhole can be expressed as

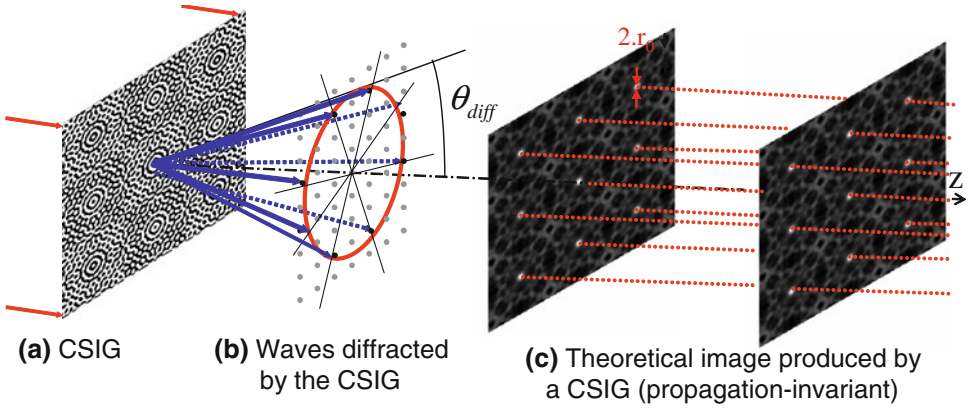

Fig. 4. Illustration of (a) a CSIG, (b) the waves diffracted by the CSIG (blue arrows, whose extremities rely on a circle), and (c) the propagation-invariant image produced by the CSIG (Color figure online).

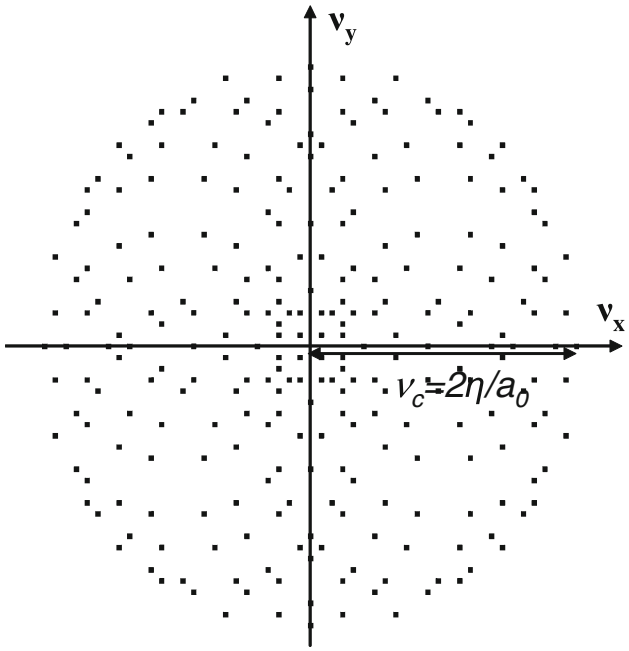

Fig. 5. Theoretical MTF of a CSIG. Each spot corresponds to an excited spatial frequency in the Fourier domain.

$$F_{\text{pinhole}}(v_x, v_y) = 2\frac{J_1(\pi\Phi'\sqrt{v_x^2 + v_y^2})}{\pi\Phi'\sqrt{v_x^2 + v_y^2}}, \tag{4}$$

where J_1 is the first-order Bessel function, and v_x and v_y stand for the spatial frequencies along two directions. Therefore, the corresponding cutoff frequency $\rho_{\text{c,pinhole}}$ is equal to

$$\rho_{\text{c,pinhole}} = \frac{1.22}{\Phi'}. \tag{5}$$

It must be higher than v_c so that the maximum frequency which can be measured with this setup remains limited by the CSIG, and not by the pinhole. By choosing $\Phi = 0.660$ mm, then $\rho_{\text{c,pinhole}} = 93$ cycles/mm, which is larger than v_c. However, filtering effects due to the pinhole slightly affect the final image (in our case, the value of the filtering function F_{pinhole} at spatial frequency $v_c = 50$ cycles/mm is equal to 0.56, which is why we correct these effects during the data processing step; see "Data Processing and Experimental Results" section). It is worth mentioning that, from a practical point of view, the diameter of the pinhole must not be too small because, in that case, the signal-to-noise ratio would decrease.

Choosing the Distance Between the CSIG and the IRFPA

From a practical point of view, CSIGs are complex objects which cannot be manufactured directly. However, a good approximation of these objects can be made with a binary-phase grating. Under polychromatic light of spectral bandwidth $\Delta\lambda$, there is a distance at which the achromatic and propagation-invariant regime is reached. This distance Z is given by Ref. 19 as

$$Z = \frac{2a_0^2}{\eta^2\Delta\lambda}. \tag{6}$$

Therefore, we have to check on our test bench that the distance d between the CSIG and the detector is greater than Z. With $\Delta\lambda = 2\mu$m, we have $Z = 1.5$ mm, and on our test bench, $d = 15$ mm, confirming that the achromatic and propagation-invariant regime is reached.

Angular Tolerance of a CSIG

In our setup, the CSIG is to be used under normal incidence. However, due to mechanical features, it can be used with a small incident angle, and we have to check that this does not affect the measurement. A study of CSIGs under oblique illumination[22] shows that the maximal incidence angle α_c of a beam illuminating a CSIG is given by

$$\alpha_c = \frac{a_0}{\eta}\left(\frac{1}{2\lambda d}\right)^{1/2}, \tag{7}$$

where λ is the illumination wavelength. For incident angles greater than α_c, the pattern produced by the CSIG suffers from off-axis aberrations (especially astigmatism) which artificially reduce the amplitude of excited spatial frequencies. Under polychromatic illumination ([3 μm; 5 μm] spectral range), we take the minimal value for the wavelength λ_{min} = 3 μm. Thus, $\alpha_{c,max}$ = 7.5° for our CSIG, which is totally compatible with mechanical constraints.

Choosing the Aperture of the IRFPA Dewar

The IRFPA is placed inside a Dewar, and we have to check that the aperture of the Dewar is sufficiently high to collect all the orders diffracted by the CSIG. As illustrated in Fig. 4b, the orders diffracted by the CSIG rely on a circle and the angle of diffraction θ_{diff} is given by

$$\sin\theta_{diff} = \lambda\frac{\eta}{a_0}. \tag{8}$$

The angle of diffraction calculated with λ = 5 μm (the longest wavelength in the spectral range of the study) is equal to θ_{diff} = 7.3°. We assume that the IRFPA is rectangular (dimensions $L \times l$, with $L > l$). The maximum angle θ_{Dewar} of an incident ray impacting the IRFPA on its edge (Fig. 6) can be calculated from the following formula:

$$\tan\theta_{Dewar} = \frac{\Phi_{cs} - l}{2h_{cs}}, \tag{9}$$

where Φ_{cs} and h_{cs} are, respectively, the diameter and height of the cold shield.

In order to collect all the orders diffracted by the CSIG, the setup has to fulfill the following condition: $\theta_{Dewar} \geq \theta_{diff}$. In our case, $\theta_{Dewar} = 10.9°$ (with the numerical values $l = 7.68$mm, Φ_{cs} = 10 mm and h_{cs} = 6 mm): the aperture of the Dewar is well suited for this experiment, and all the diffracted orders will impact the IRFPA.

The test bench we have designed is illustrated in Fig. 7.

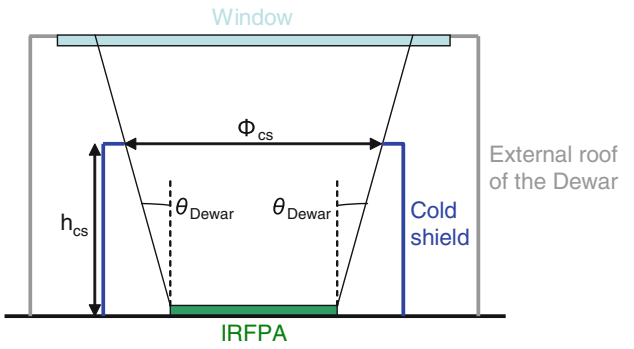

Fig. 6. Mechanical characteristics of the Dewar.

DATA PROCESSING AND EXPERIMENTAL RESULTS

The image acquired by the IRFPA is shown in Fig. 8. We have developed a data processing method to extract the MTF information from the experimental image for each zone; each zone is processed separately.

General Description of Data Processing

The approach which has been developed consists in a parametric estimation of the MTF, that is to say, a maximum-likelihood estimation of a set of unknown parameters. It consists in two main steps. First, we need to define and to compute a model image for any set of the parameters which describe the problem (including those which specifically describe the MTF). Then, we find the set of parameters which maximizes the similarity between the recorded experimental image i and the model image m_0. The similarity metric is deduced from the noise statistics.

In a recorded image, the unknown parameters are:

1. The period a_0 of the CSIG, which is linked to the distance between two consecutive bright spots in the Fourier domain

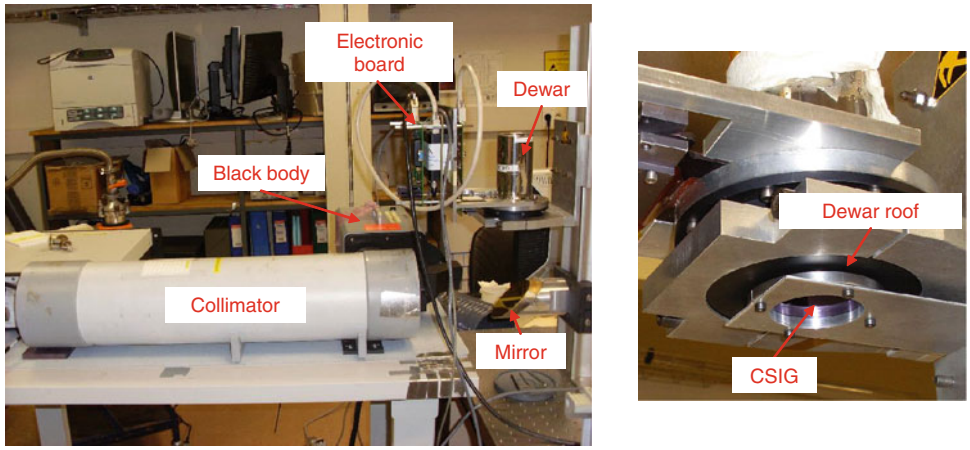

Fig. 7. Photographs of the test bench.

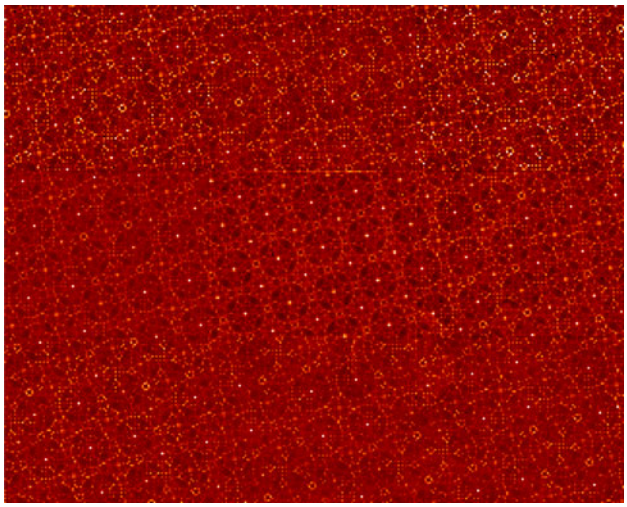

Fig. 8. CSIG pattern acquired by the IRFPA (with integration time adapted for each area, so that the mean value of each area is kept almost constant).

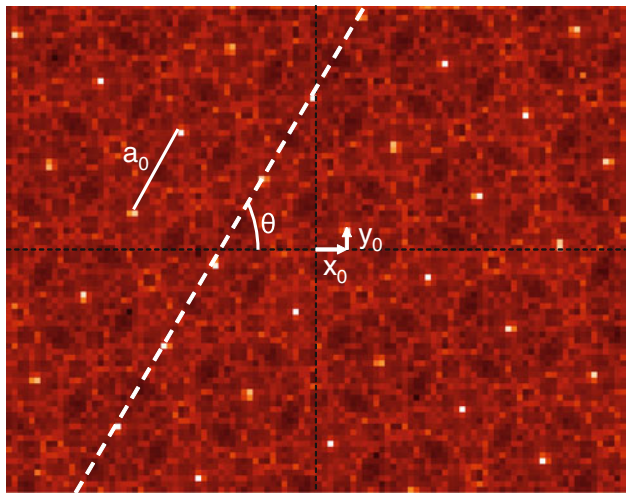

Fig. 9. Illustrations of the parameters a_0, θ, x_0, and y_0.

2. The angle θ between the CSIG pattern and the pixel lines of the IRFPA
3. The position (x_0, y_0) of the center of the CSIG pattern with respect to the center of the image
4. The flux G of the image
5. A possible offset O_{ff} of the image
6. Several parameters (gathered in the vector $\mathbf{p}$) which describe the pixel filtering function: these are the parameters of interest in our problem

The parameters a_0, θ, x_0, and y_0 are illustrated in Fig. 9.

For unit flux and zero offset, the model image m_0 is generated in the Fourier domain, and then the real image is calculated with an inverse Fourier transform. We note that $\tilde{m}_0$, the Fourier transform of m_0, is given by

$$\begin{aligned}\tilde{m}_0(v_x, v_y) = F_{\text{CSIG}}(v_x, v_y) \times \exp(-2j\pi(v_x x_0 + v_y y_0)) \\ \times F_{\text{pinhole}}(v_x, v_y) \times F_{\text{diode}}(v_x, v_y),\end{aligned} \tag{10}$$

where $F_{\text{CSIG}}(v_x, v_y)$ is the transfer function of an ideal CSIG pattern of period a_0 and angle θ, and $F_{\text{diode}}(v_x, v_y)$ is a function which accounts for the pixel filtering effects.

A very simple model for filtering effects has been proposed as a first approach: the diode is described as a disk of diameter Φ_{diode}. Therefore, the filtering function F_{diode} is of the form

$$F_{\text{diode}}(v_x, v_y) = 2\frac{J_1\left(\pi\Phi_{\text{diode}}\sqrt{{v_x}^2 + {v_y}^2}\right)}{\pi\Phi_{\text{diode}}\sqrt{{v_x}^2 + {v_y}^2}}. \tag{11}$$

The optimization process seeks the optimal value of Φ_{diode}.

For the zone of standard pixels with fill factor equal to 1 (zone 5), we have used another filtering function which accounts for square pixels of size t_{pix}, i.e.,

$$F_{\text{diode}}(v_x, v_y) = \sin c(t_{\text{pix}} v_x) \times \sin c(t_{\text{pix}} v_y), \tag{12}$$

where $\sin c$ is a function defined by $\sin c(x) = 1$ if $x = 0$ and $\sin c(x) = \frac{\sin(\pi x)}{\pi x}$ otherwise. In this case, the optimization process seeks the optimal value of t_{pix}.

In our work, we assume that the noise is Gaussian and nonhomogeneous, which is a good approximation for a mixture of photon and detection noises.[23] With this assumption, the maximum-likelihood method boils down to a weighted least-squares method, where the weights $w(k, l)$ are the inverses of the noise variance at each pixel (k, l). From a practical point of view, we use a binary matrix for w (0 for dead pixels, 1 for other pixels). Then, the maximum-likelihood method implies minimizing the following criterion J:

$$\begin{aligned}J(a_0, \theta, x_0, y_0, \mathbf{p}, G, O_{\text{ff}}) = \frac{1}{2}\sum_{k,l} w(k,l) \cdot | \, i(k,l) \\ - [G \cdot m_0(k, l, a_0, \theta, x_0, y_0, \mathbf{p}) \\ + O_{\text{ff}}] \, |^2,\end{aligned} \tag{13}$$

where i is the experimental image.

The criterion J is a quadratic function of G and O_{ff}, thus an analytical solution $(\hat{G}(a_0, \theta, x_0, y_0, \mathbf{p}), O_{\text{ff}}(a_0, \theta, x_0, y_0, \mathbf{p}))$ can be found for the minimization of J, for a given set of other parameters a_0, θ, x_0, y_0, and $\mathbf{p}$. This analytical solution is found by solving the following matrix system:

$$MX = C, \tag{14}$$

with

$$M = \begin{pmatrix} \sum_{k,l} w(k,l) m_0^2(k,l) & \sum_{k,l} w(k,l) m_0(k,l) \\ \sum_{k,l} w(k,l) m_0(k,l) & \sum_{k,l} w(k,l) \end{pmatrix}, \tag{15}$$

Table II. Values of the parameter Φ_{diode} for zones with small diodes

Zone	1	2	3	4	5	6	7	8	9
Diode diameter (μm)	14.7	12.6	11.2	20.6	–	21.0	14.1	12.3	11.3

$$X = \begin{pmatrix} \hat{G} \\ \hat{O}_{\text{ff}} \end{pmatrix}, \tag{16}$$

and

$$C = \begin{pmatrix} \sum_{k,l} w(k,l) i(k,l) m_0(k,l) \\ \sum_{k,l} w(k,l) i(k,l) \end{pmatrix}. \tag{17}$$

X is calculated by inverting M: $X = M^{-1}C$.

Thus, a faster and simpler way to minimize J consists in minimizing the criterion J' defined by the following equation, where we have introduced the analytic expressions $\hat{G}$ and $\hat{O}_{\text{ff}}$:

$$J'(a_0,\theta,x_0,y_0,\mathbf{p}) = J(a_0,\theta,x_0,y_0,\mathbf{p},\hat{G}(a_0,\theta,x_0,y_0,\mathbf{p}), \hat{O}_{\text{ff}}(a_0,\theta,x_0,y_0,\mathbf{p})). \tag{18}$$

To minimize the criterion J', we used the Levenberg–Marquardt method, written in IDL language,[24] as implemented in the reference software MINPACK-1 developed by Moré et al.[25,26]

The optimization process was carried out for each zone. For zone 5, the optimal parameter is found to be $t_{\text{pix}} = 29\mu$m. This value is close to the size of a standard square pixel (30μm), which means that the optimization process is satisfactory. For the zones with small fill factor, the values of the optimized parameter Φ_{diode} are given in Table II.

As there is no confinement ring for zones 4 and 6, we notice that the size of the diodes in these zones is significantly larger than in the other zones. The explanation for this phenomenon could be that the physical diameter of the diode is equal to the diode diameter added to twice the diffusion length. The diffusion length depends on the material, and for the IRFPA under study, it is approximately equal to 9 μm. Then, the results are in accordance with this model.

We assume that the MTF is radial, because the diodes have been implanted on circles (except for the central zone 5, where the pixels are square). Then, we plot the filtering function F_{diode} (with the optimized parameter Φ_{diode}) as a function of radial spatial frequency $\sqrt{v_x^2 + v_y^2}$ for each small fill factor zone. These curves are shown in Fig. 10.

CONCLUSIONS

We have designed an original test bench for MTF measurement based on a diffraction grating called a CSIG. This method is particularly well suited for MTF measurement of cooled IRFPAs which are integrated in a Dewar, since no precise working distance between the CSIG and the FPA has to be respected; however, it could also be extended to MTF measurement of FPAs working in the visible spectral range, potentially with very small pixel size. We have also developed data processing based on a parametric approach devoted to this measurement method. Consideration of a simple function to model the filtering effects of the diodes provides encouraging results.

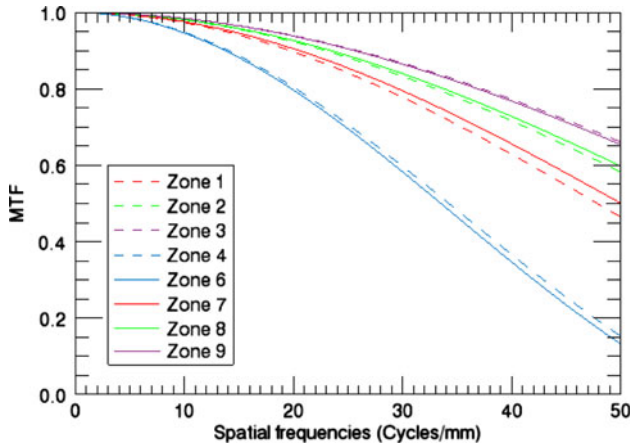

Fig. 10. Filtering functions F_{diode} plotted with the optimized parameter Φ_{diode} for each small fill factor zone.

In future work, we will measure MTFs at higher spatial frequencies (up to 100 cycles/mm) with a new CSIG. We will also look for a more general filtering model to account for potential nonsymmetrical effects inside the diode. We could extract a two-dimensional MTF, and then apply a reverse Fourier transform to retrieve a two-dimensional profile of the diode: this would be the point spread function of the diode. We will also compare the obtained results with the physical features of the diodes.

ACKNOWLEDGEMENTS

This project was sponsored by the DGA, the French procurement agency.

REFERENCES

1. S.E. Reichenbach, S.K. Park, and R. Narayanswamy, *Opt. Eng.* **30**, 170 (1991).
2. M.A. Chambliss, J.A. Dawson, and E.J. Borg, *Proc. SPIE* **2470**, 312 (1995).
3. M. Estribeau and P. Magnan, *Proc. SPIE* **5251**, 243 (2004).
4. G.C. Holst, *Infrared and Electro-optical Systems Handbook*, vol. 4, ed. M.C. Dudzik (Ann Arbor, MI: Environmental Research Institute of Michigan, 1993), pp. 223–232.

5. J.D. Bray, L.W. Schumann, and T.S. Lomhein, *Proc. SPIE* **7405**, 74050Q (2009).
6. M. Marchywka and D.G. Socker, *Appl. Opt*. **31**, 7198 (1992).
7. J.E. Greivenkamp and A.E. Lowman, *Appl. Opt*. **33**, 5029 (1994).
8. R.O. Gappinger, J.E. Greivenkamp, and C. Borman, *Opt. Eng*. **43**, 689 (2004).
9. G. Boreman and E.L. Dereniak, *Opt. Eng*. **25**, 148 (1986).
10. M. Sensiper, G.D. Boreman, A.D. Ducharme, and D.R. Snyder, *Opt. Eng*. **32**, 395 (1993).
11. X. Chen, N. George, G. Agranov, C. Liu, and B. Gravelle, *Opt. Express* **16**, 20047 (2008).
12. B.T. Teipen and D.L. MacFarlane, *Appl. Opt*. **39**, 515 (2000).
13. M. Chambon, J. Primot, and M. Girard, *Infrared Phys. Technol*. **37**, 619 (1996).
14. D.N. Sitter Jr, J.S. Goddard, and R.K. Ferrell, *Appl. Opt*. **34**, 746 (1995).
15. N. Guérineau, J. Primot, M. Tauvy, and M. Caes, *Appl. Opt*. **38**, 631 (1999).
16. N. Guérineau, J. Primot, M. Tauvy, and M. Caes, *Proc. SPIE* **3491**, 826 (1998).
17. N. Guérineau and J. Primot, *J. Opt. Soc. Am. A* **16**, 293 (1999).
18. N. Guérineau, B. Harchaoui, J. Primot, and K. Heggarty, *Opt. Lett*. **26**, 411 (2001).
19. N. Guérineau, S. Rommeluère, E. Di Mambro, I. Ribet, and J. Primot, *C.R. Phys*. **4**, 1175 (2003).
20. E. Di Mambro, N. Guérineau, and J. Primot, *Proc. SPIE* **5076**, 169 (2003).
21. J. Durnin, *J. Opt. Soc. Am. A* **4**, 651 (1987).
22. G. Druart, N. Guérineau, R. Haïdar, J. Primot, P. Chavel, and J. Taboury, *J. Opt. Soc. Am. A* **24**, 3379 (2007).
23. L.M. Mugnier, T. Fusco, and J.-M. Conan, *J. Opt. Soc. Am. A* **21**, 1841 (2004).
24. C.B. Markwardt, *Astronomical Data Analysis Software and Systems XVIII*, ed. D.A. Bohlender, D. Durand, and P. Dowler (San Francisco: ASP, 2009), p. 251.
25. J.J. Moré, *Numerical Analysis* (Berlin: Springer, 1978), pp. 105–116.
26. J.J. Moré, B. S. Garbow, and K. E. Hillstrom, User guide for MINPACK-1, Technical report Argonne National Laboratory ANL-8-74 (Argonne, IL, USA, 1980).